A multimodal microcharacterisation of trace-element zonation and crystallographic orientation in natural cassiterite by combining cathodoluminescence, EBSD, EPMA and contribution of confocal Raman-in-SEM imaging

Guillaume Wille, Catherine Lerouge, U. Schmidt

Journal of
Microscopy

Journal of Microscopy, Vol. 270, Issue 3 2018, pp. 309–317
Received 16 June 2017; accepted 29 December 2017
doi: 10.1111/jmi.12684

A multimodal microcharacterisation of trace-element zonation and crystallographic orientation in natural cassiterite by combining cathodoluminescence, EBSD, EPMA and contribution of confocal Raman-in-SEM imaging

G. WILLE*, C. LEROUGE* & U. SCHMIDT†
*BRGM, 3 Avenue Claude Guillemin, Orleans, Cedex 2, France
†WITec GmbH, Lise-Meitner-Straße 6, Ulm, Germany

Key words. Cassiterite, cathodoluminescence, EBSD, EPMA, Raman-in-SEM, RISE, SEM.

Summary

In cassiterite, tin is associated with metals (titanium, niobium, tantalum, indium, tungsten, iron, manganese, mercury). Knowledge of mineral chemistry and trace-element distribution is essential for: the understanding of ore formation, the exploration phase, the feasibility of ore treatment, and disposal/treatment of tailings after the exploitation phase. However, the availability of analytical methods make these characterisations difficult.

We present a multitechnical approach to chemical and structural data that includes scanning electron microscopy (SEM)-based imaging and microanalysis techniques such as: secondary and backscattered electrons, cathodoluminescence (CL), electron probe microanalyser (EPMA), electron backscattered diffraction (EBSD) and confocal Raman-imaging integrated in a SEM (RISE). The presented results show the complementarity of the used analytical techniques. SEM, CL, EBSD, EPMA provide information from the interaction of an electron beam with minerals, leading to atomistic information about their composition, whereas RISE, Raman spectroscopy and imaging completes the studies with information about molecular vibrations, which are sensitive to structural modifications of the minerals. The correlation of Raman bands with the presence/absence of Nb, Ta, Fe (heterovalent substitution) and Ti (homovalent substitution) is established at a submicrometric scale. Combination of the different techniques makes it possible to establish a direct link between chemical and crystallographic data of cassiterite.

Correspondence to: Wille Guillaume BRGM, 3 Avenue Claude Guillemin, BP 36009, 45060 ORLEANS Cedex 2, France. Tel: +33 (0)238643522; fax +33 (0)238643711; e-mail: g.wille@brgm.fr

Introduction

Cassiterite (SnO_2) has been and continues to be the most important source of tin (Sn). Sn is also associated with other metals such as titanium (Ti), niobium (Nb), tantalum (Ta), indium (In) and tungsten (W), which can complicate ore treatment, although some of these metals can be extracted as by-products. A detailed knowledge of mineral chemistry and trace element distribution is necessary in the exploration phase for: a better understanding of ore formation, ore treatment feasibility and tailings disposal after the exploitation phase.

Cassiterite crystallises in the tetragonal system with a space group of D41h4- P 4/mnm. Because of its rutile-type structure, cassiterite can incorporate significant amounts of Ti, and also trace elements. Similar to rutile, natural cassiterite can incorporate Fe, Mn, Nb, Ta, In, W and Hg (Cerny *et al.*, 1985; Izoret *et al.*, 1985; Giuliani, 1987; Möller *et al.*, 1988; Neiva, 1996; Murciego *et al.*, 1997; Botelho & Moura, 1998; Serranti *et al.*, 2002; Briskey, 2005; Lerouge *et al.*, 2007). Characterisation of cassiterite remains a challenge for analytical techniques. EPMA is lacking due to interference of Sn and trace elements. X-ray emission lines of In Lα, Ta Mα in wavelength-dispersive X-ray spectroscopy (WDS) can only be solved by the use of less intense bands (Ta Mβ or Lα for example). SEM is required due to the nanometric size of the zonation areas, however, the BSE detector is often not sensitive enough for the detection of the low content of trace elements. Cathodoluminescence in the SEM however reveals the trace elements distribution.

Raman spectroscopy measures the vibrational frequencies of molecular bonds in a material. The resulting Raman spectrum is not only unique for a given compound, but is also sensitive to the local environment. The spectrum reveals structural data; it provides details on the chemical and structural properties (nature of the functional groups, symmetry group, lattice defects etc.) and the crystallinity of mineral compounds.

This method offers a variety of analytical possibilities that include, among others, identification of different polymorphs (Hope *et al.*, 2001; Gao *et al.*, 2009), determination of different oxidation states (Das & Hendry, 2011) and crystallographic orientations (Mossbrucker & Grotjohn, 1996), evaluation of temperature (Lahfid *et al.*, 2010) and stress effects on crystal and molecular structure (Mossbrucker & Grotjohn, 1997).

The availability of Raman spectroscopy in a SEM equipped with imaging detector [secondary electrons (SE), backscattered electrons (BSE), cathodoluminescence (CL) etc.] and microcharacterisation (EDS, WDS, EBSD) allows morphological, elemental, chemical, and physical studies without transferring the sample from one instrument to another. Commercial systems have been available for about 15 years. These systems use an 'on-axis' configuration, that is a parabolic mirror is inserted under the pole piece of the SEM to carry the laser beam to the sample surface and to collect diffused light for spectroscopic analysis (Wille *et al.*, 2014). The mirror is connected through a special interface to a conventional μ-Raman spectrometer. The advantage of such a system has been established for different applications, including forensic applications (Otieno-Alego, 2009) and characterisation of individual particles (Worobiec *et al.*, 2010; Stefaniak *et al.*, 2014; Pointurier and Marie, 2010; Nelson *et al.*, 2001), biological samples (Jarvis & Goodacre, 2004; Jarvis *et al.*, 2004) and mineralogical samples (Stefaniak *et al.*, 2009; Maubec *et al.*, 2013).

Another Raman-in-SEM configuration has been proposed (Van Apeldoorn *et al.*, 2005) and a commercial version is available, but it is affected by several limitations (in particular, a limited spectral range). A similar configuration, named 'RISE' (Raman Imaging and Scanning Electron microscopy) has been developed by manufacturers Tescan (SEM) and Witec (Raman) and major improvements have been proposed to address the former on-axis configuration (Jiruse *et al.*, 2014). This new configuration, which can be defined as a 'parallel setup', entails the use of a precise stage and an image repositioning tool to transfer the sample in the SEM chamber from an SEM position (under the pole piece) to a Raman position (under the Raman objective). Unlike the 'on-axis' setup, the parallel setup makes it possible to collect Raman spectra without any intensity loss compared to a conventional μ-Raman equipped with the same optical objective. Moreover, Raman mapping is possible through the collection of a 'data cube' (one spectrum collected for each pixel of the optical image) at high speed (Jiruse *et al.*, 2014).

For this study, cassiterite from the Cadomian Montbelleux Sn ±W ore deposit has been selected because of the millimetric- to centimetric-size and the euhedral forms of the crystals, its high concentrations of rare metals including Nb, Ta, Fe, Ti, In and W, and strong chemical zoning compared to cassiterite from Variscan Sn ore deposits in Brittany, French Massif Central and Galicia (Lerouge *et al.*, 2017). The substitutions in rare metals were discussed, but their distribution remains unknown at the crystal scale. This paper presents a complementary multitechnical approach to chemical and structural data that was tested on cassiterite crystal specimens from Montbelleux to provide a better characterisation of chemical zoning; the approach includes scanning electron microscopy (SEM), cathodoluminescence in-SEM imaging (CL), electron probe microanalysis (EPMA) and electron backscattered diffraction (EBSD).

The contribution and features introduced by coupling SEM and Raman spectroscopy in a coupled SEM-confocal micro-Raman imaging and spectroscopy (RISE) are highlighted.

Material and methods

Materials

Montbelleux is located at Luitré (Ille-et-Vilaine, France) in the Cadomian belt of northern Brittany, and more precisely in the Mancellian Domain (Ballèvre *et al.*, 2001) (Fig. 1). Mineralisation occurs as quartz–cassiterite–wolframite stockwork in a greisen topaz-bearing sodic granite dated at 490 ± 15 Ma by Rb–Sr isochron (Rossi *et al.*, 1988) and as quartz–wolframite veins in schist at the contact with the batholith (Chauris *et al.*, 1989). Cassiterite from greisen granite, previously analysed for trace elements using EPMA, is rich in Fe, Nb, Ta, Ti, compared to other Variscan Sn deposits in Brittany (Lerouge *et al.*, 2017) (Table 1). Additionally the morphology of the crystals is of significant interest. Such samples, containing millimetric cassiterite grains, were selected and prepared as polished sections for mineralogical investigations (Fig. 2).

Methods

Electron beam microscopy and microcharacterisation techniques. Polished sections were observed in the SEM, under low vacuum conditions (uncoated samples) for EBSD and RISE and high vacuum conditions (carbon-coated samples) for CL and EPMA. Elemental mapping and quantitative analyses were performed using EPMA on carbon-coated polished sections. Carbon-coated polished sections were coated with 20 nm carbon using a Cressington 308 (Cressington, Watford, UK).

SEM images were obtained using a Tescan Mira 3 XMU (Tescan, Brno, Czech Republic) equipped with a secondary electron (SE) Everhart-Thornley detector (Everhart & Thornley, 1960) for high vacuum SE imaging, a low vacuum (LV) SE detector (Jacka *et al.*, 2003) for LV–SE imaging and a YAG-scintillator backscattered electron (BSE) detector (Autrata-type BSE detector – Autrata, 1992) at HV = 25 kV and a panchromatic cathodoluminescence detector (350–650 nm) (TESCAN BSE/CL detector). Low vacuum mode (LV) was used, with P = 20 Pa nitrogen.

Orientation maps were obtained using an Edax Pegasus system with a Digiview IV camera and OIM DC 6.4 software

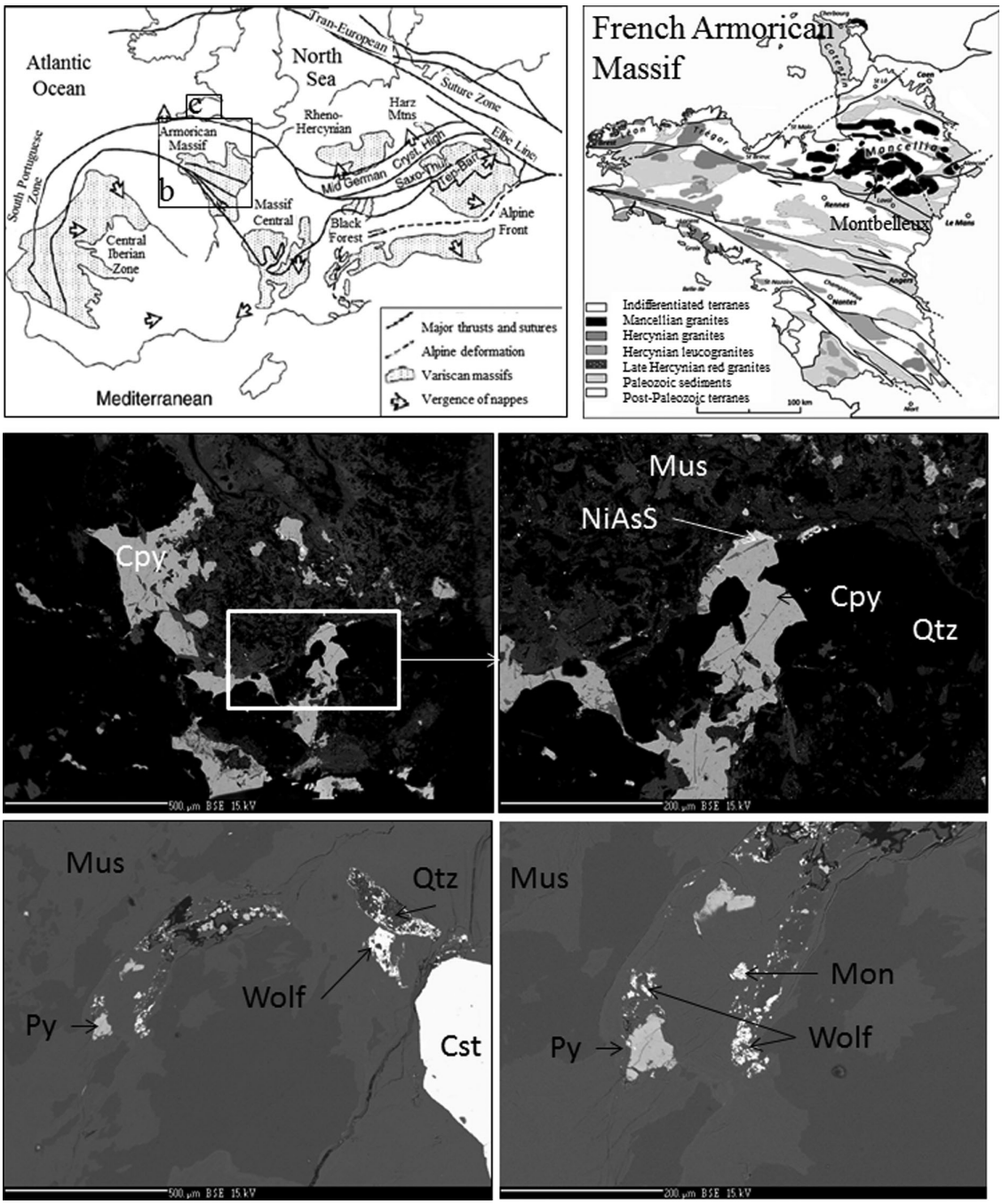

Fig. 1. Location of Montbelleux deposit and SEM (BSE) images of the cassiterite surrounding minerals (after Lerouge *et al.*, 2017).

(Edax, Mahwah, USA). Collection was done on noncoated samples at HV = 25 kV, under low vacuum conditions (P = 20 Pa Nitrogen). Samples had been previously polished using a high-quality protocol including a colloidal silica final step.

Wavelength-dispersive X-ray spectroscopy (WDS) elemental mapping was performed on a Cameca SXFive electron microprobe (Cameca, Gennevilliers, France) using an accelerating voltage of 20 kV and a beam current of 200 nA. Complementary spot analyses were performed using an accelerating voltage of 20 kV and intensity of 50 nA to quantify the amount of Nb, Ta, Ti, Fe and W. Ti Kα, Sn Lα, Nb Lα were measured on PET (pentaerythritol, $2d = 8.74$ Å), Fe Kα, on LiF (Lithium fluoride, $2d = 4.0267$ Å) and Ta Mβ, W Lα on TAP (thallium acid phtalate, $2d = 25.75$ Å). Counting time was 10 s for Ti, Fe, and Mn and 40 s for the other elements. Standards of calibration for EPMA spot quantitative

Table 1. Average contents of main trace elements in cassiterite from Montbelleux by EPMA (after Lerouge *et al.*, 2007).

Number of analyses		SnO_2 wt %	Trace element contents (mg kg^{-1}) Fe	In	Nb	Ta	Ti
45	Average	98.97	2568	519	3901	5809	2635
	std. dev.	0.74	1402	204	3487	4325	1377

$Sn_{2.92\pm0.04}$ $Fe_{0.02\pm0.01}$ $Nb_{0.02\pm0.02}$ $Ta_{0.01\pm0.01}$ $Ti_{0.02\pm0.01}$ O_2

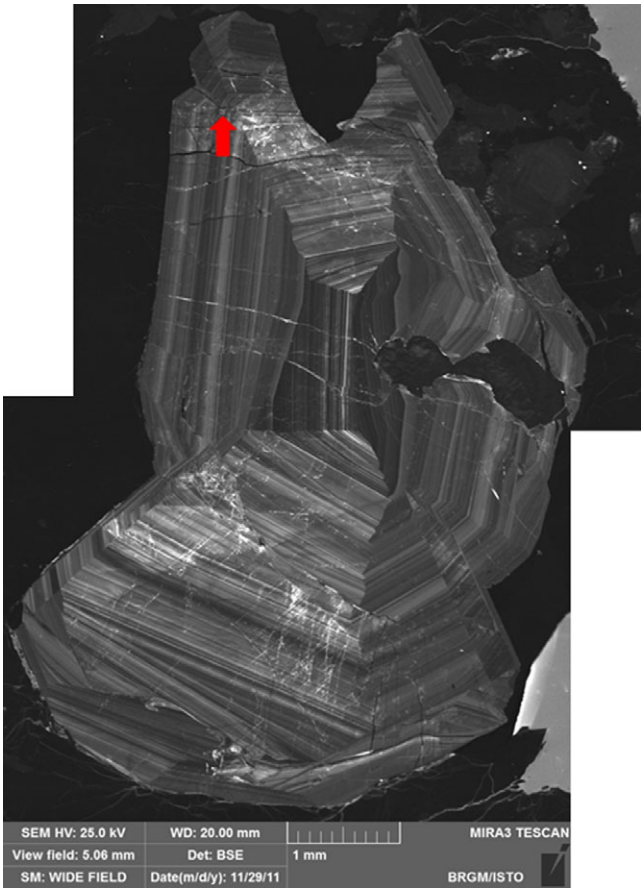

Fig. 2. SEM – panchromatic cathodoluminescence image of a centimetric cassiterite grain (red arrow: position of analysed area – see Fig. 3).

analyses are natural minerals: cassiterite for Sn, synthetic oxides: MnTiO3 for Ti and Fe2O3 for Fe, and pure elements: Nb, Ta and W metals. The detection limits of the elements for a single analysis, given in mg kg^{-1}, are for Ti, Fe, Sn, Ta, In and Nb in Table 1.

RISE Raman imaging in the SEM. Informations on the local chemistry of zoned cassiterite can be obtained at a submicrometric scale using Confocal Raman spectroscopy and Imaging. Confocal Raman imaging was performed on a Tescan-Witec RISE microscope combining a Tescan Mira SEM integrated with a Witec Confocal Raman Imaging System (Witec, Ulm, Germany). The RISE confocal Raman imaging system is equipped with a UHTS300 spectrometer, a Zeiss 100 × vacuum objective (N.A. 0.75) mounted inside the SEM chamber, using a 532 nm laser excitation wavelength (Jiruse *et al.*, 2014).

Results and discussion

Zonation and crystal orientation in cassiterite grains using SE, CL, EBSD and EPMA

Cassiterite has been extensively studied with cathodoluminescence (CL) to elucidate processes of crystal growth (Farmer *et al.*, 1991). CL imaging of a centimetric cassiterite grain from Montbelleux, acquired in SEM, provides evidence of intense contrast variations (Fig. 2). These contrasts can be attributed to very fine chemical zoning in trace elements (Hall & Ribbe, 1971; Remond, 1973; Remond *et al.*, 1992) and to crystal orientations which are known to strongly affect cathodoluminescence in cassiterite (Hall, 1978).

To decrypt the origin of the CL contrast, a small area highlighted with the red arrow in Figure 2 (Fig. 3) was analysed with various techniques. Figure 4 shows the EBSD inverse pole figure (IPF) map (Fig. 4A), the corresponding CL image (Fig. 4B) and the inverse pole figure projection (Fig. 4C), acquired from an area of 253 × 190 μm^2. The EBSD IPF map was collected with a step of 1 μm. A cleaning procedure (grain dilation) was applied to remove mis-indexed points. The CL and EBSD images show identical contrasts. Both images show the presence of cracks, the only topographic features on a polished surface. The change of grey in the SE image (Fig. 2) corresponds to an orientation contrast due to electron channelling, a phenomenon that occurs in a crystal due to the interaction between primary electrons and the crystal structure (Lloyd, 1987). A similar change is observed also in the EBSD image, providing evidence of mono-oriented grains with twinning. Twinning is well known in cassiterite as the 'elbow twin' (Nespolo & Souvignier, 2015). An orientation variation of 68° was measured between the twin and the main orientation of the centimetric grain (Fig. 4A), which is close to 70°, the ideal structure (Nespolo & Souvignier, 2015).

The CL image (Fig. 4B) shows in addition the presence of alternating dark and bright bands which are associated with chemical zoning due to the incorporation of trace elements.

A comparison of the three images in Figure 4 reveals that the alternating bands in the CL image are parallel to the crystal faces and change their orientation in the corresponding twin crystals.

Trace element mapping was conducted by EPMA. EPMA trace element analysis is challenging due to the existence of interferences between the detectable trace elements. For example, tantalum (Ta), an element detected in this cassiterite grain, can be analysed on the Mα line, which has the highest

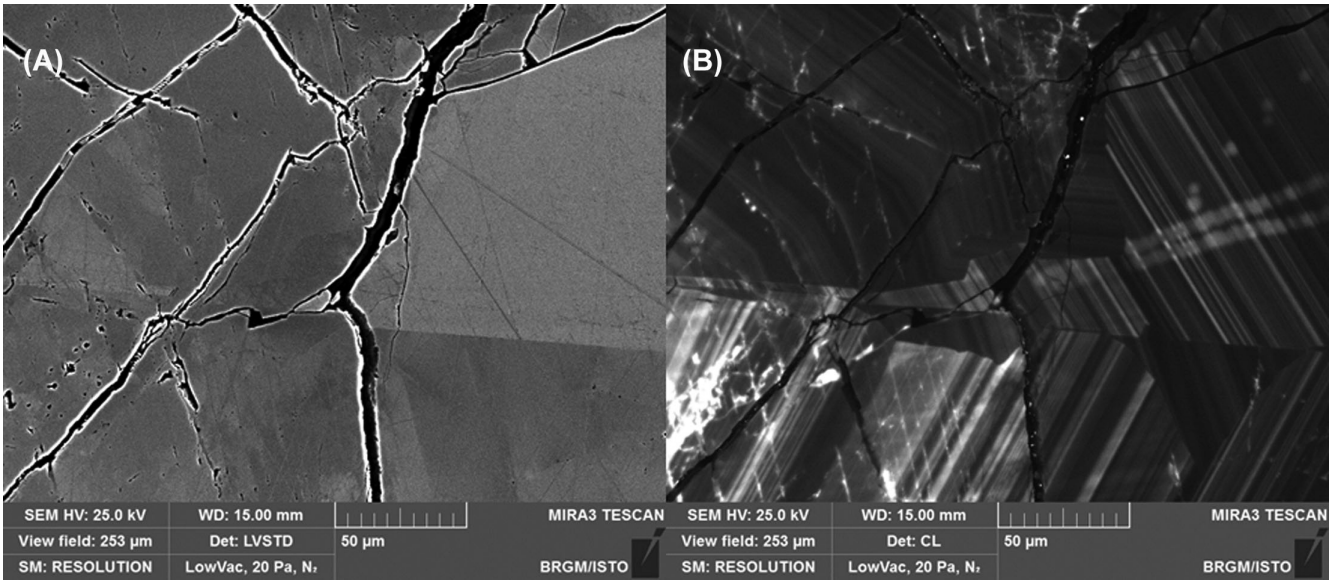

Fig. 3. Secondary electrons (A) and panchromatic cathodoluminescence (B) images of the cassiterite grain area.

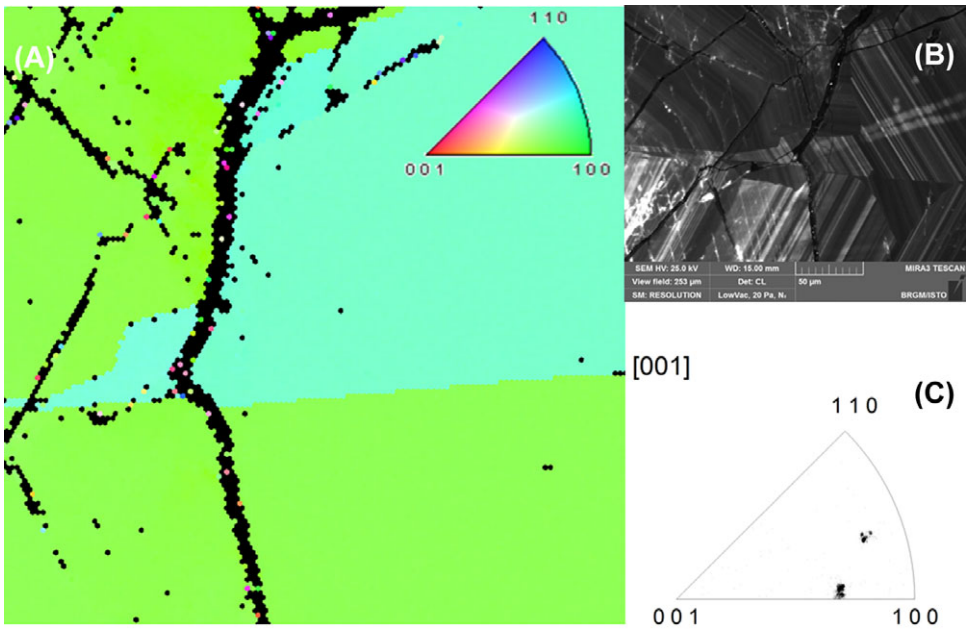

Fig. 4. EBSD orientation map of the area of interest (A), CL image (B) and [001] inverse pole figure (C).

intensity at HV = 15–30 kV. However, interference occurs between Ta Mα and Sn L$\alpha^{(2nd\ order)}$ peaks on a TAP monochromator (Fig. 5). The use of the differential mode is a good opportunity to remove the contribution of this Sn L$\alpha^{(2nd\ order)}$ peak when the differential mode window is set to 3 V. A small contribution is still evident (about 1.5 × background level in SnO_2). A further reduction of the width of the differential mode window (lower than 800 mV) is not able to completely remove the 2nd-order contribution. It leads to a greatly reduced peak intensity, which can be detrimental for trace analysis. As a result, Ta was collected on Ta Lα at 8.145 KeV. These results are presented in Table 2, where only detected elements are reported.

Elemental mapping was performed by EPMA (WDS spectrometers) on the same area than Cl and EBSD. Experimental conditions were determined to highlight trace element distribution. Elemental maps were collected at HV = 20 kV and beam current = 200 nA, map resolution = 512 × 512 pixels (stage scanning, step = 1 μm). Like CL image, elemental mapping of trace elements provides evidence of complex chemical zoning of Nb, Ti, Ta and Fe. EPMA (WDS)

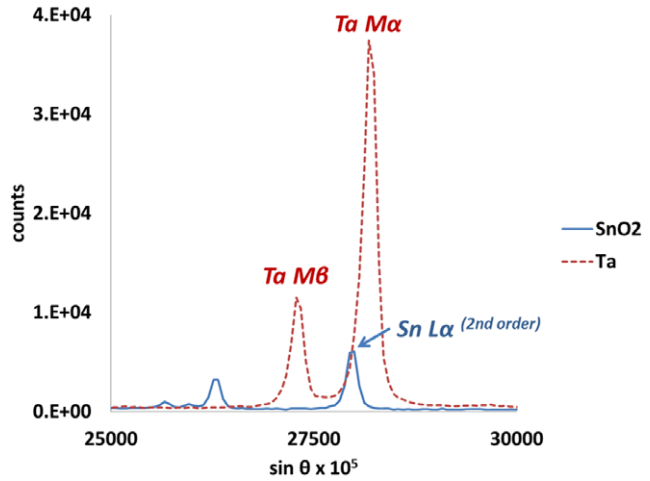

Fig. 5. WDS interference Ta Mα/Sn Lα (2nd order) on a TAP monochromator.

Table 2. Average contents of main trace elements in the different area identified by RISE microscopy (from EPMA analyses). Detection limit (in %) for each element is given in brackets.

Area	TiO_2 (0.03)	FeO (0.035)	Nb_2O_5 (0.018)	SnO_2 (0.163)	Ta_2O_5 (0.050)
a	0.405	0.061	0.114	99.413	0.000
c	0.612	0.083	0.043	99.223	0.000
d	0.531	0.082	0.329	99.009	0.050

maps (peak intensity) for Ta, Nb, Fe and Ti are presented in Figures 6(C)–(F) and compared with SEM-CL and RISE images obtained from the same sample area. The main zonation domains are surrounded by white lines to highlight the correspondence between trace element distribution, CL contrast and Raman spectral variations. According to Table 2, Ti is the most abundant trace element and is regularly distributed in large Ti-rich bands alternating with fine Ti-poor bands corresponding to crystal growth. Nb and Fe are less abundant with the same order of content, according to EPMA analyses. On the contrary, Nb is more heterogeneously distributed throughout the cassiterite crystal (Fig. 6D), with irregular domains that are chemically zoned and highly enriched in Nb, and other crystal domains that are not clearly zoned and are poorer in Nb. The distribution of these domains compared to the EBSD map (Fig. 5) also provides evidence of a line probably corresponding to the limit of the twinning. Ta is present at very low concentrations (Table 2). Comparison of the different elemental maps indicates that some rare Ta-rich bands seem to correspond to Nb-rich bands, and Ti-depleted bands to Fe-rich bands.

The cathodoluminescence properties of cassiterite depend to a great degree on trace elements content (Hall & Ribbe, 1971; Remond, 1973; Farmer *et al.*, 1991). The CL image of

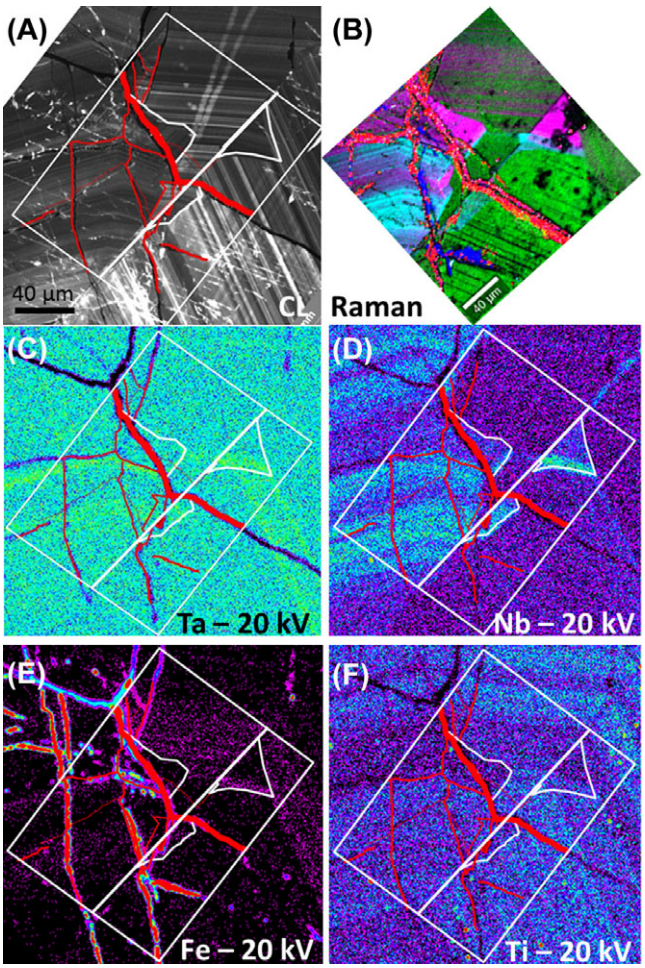

Fig. 6. comparison of cathodoluminescence image (CL) (A) and RISE imaging map (B) with elemental mapping for trace elements Ta (C), Nb (D), Fe (E) and Ti (F). Fissures are indicated in red. White lines give limits of small domains presenting different orientations of growth and low luminescence.

the mapped area confirms the relationship between crystal growth and trace element distribution (Fig. 6). However, the relationship between trace element distribution and luminescence is complex. The Fe-rich zones seem to correspond to very low luminescence, and luminescence is quenched when Ti is associated with Fe.

Ti acts as an activator, whereas luminescence is quenched when Fe is present with Ti. The influence of Ti on the CL activation is shown in various places in this area. Furthermore, Nb and Ta may turn out to have a negative effect on the panchromatic cathodoluminescence intensity. However, in numerous places in the observed area, Ti is associated with Nb and/or (Nb + Ta), elements that act as quenchers of cathodoluminescence, so that CL intensity prediction is difficult if not impossible. A general observation is that luminescence in the range of 330–660 nm clearly decreases with increase of the Nb and Ta concentration.

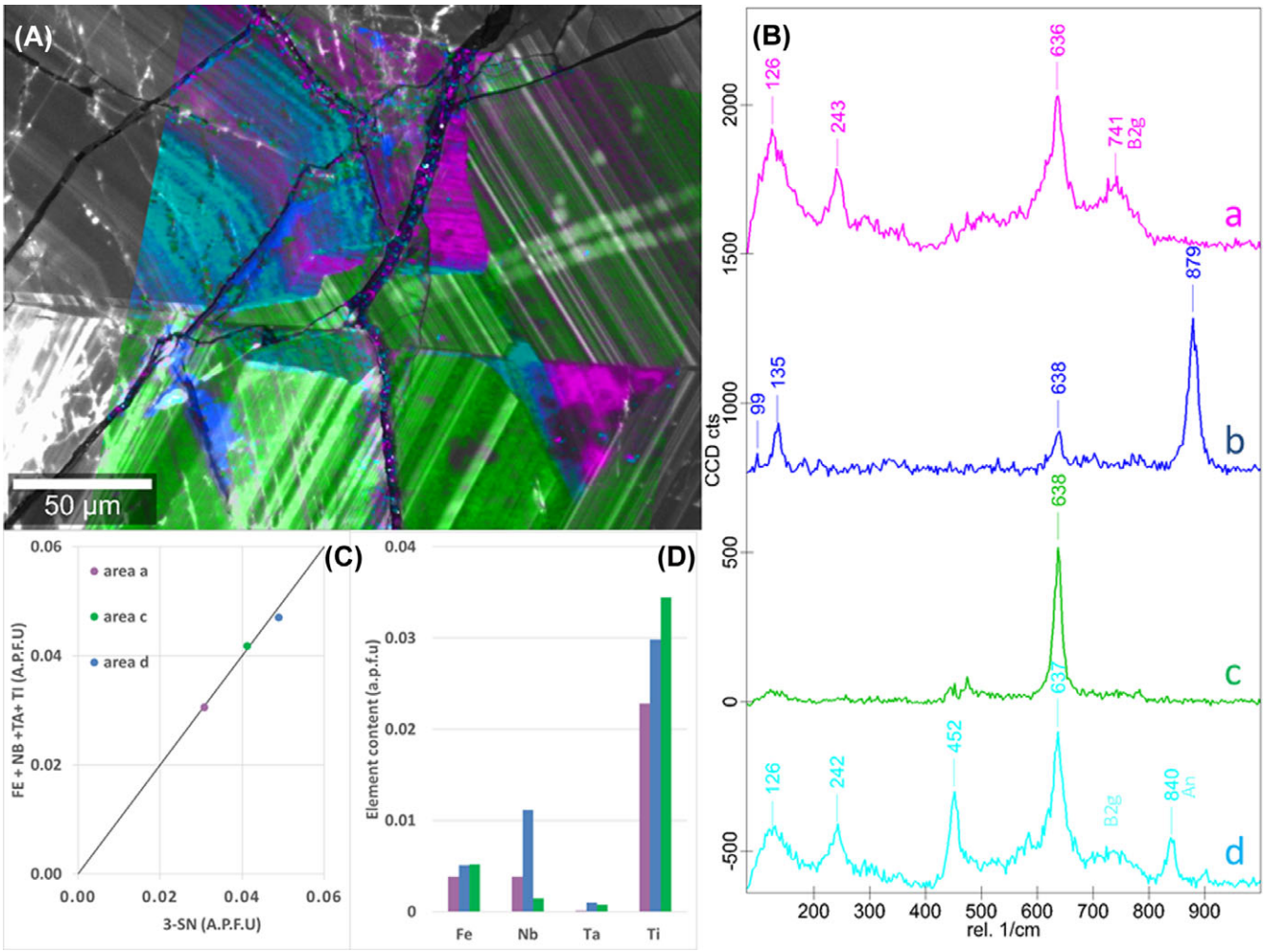

Fig. 7. Raman map superimposed on CL image (A) and Raman spectrum of each area identified on the Raman map (B), 1:1 correlation between 3-Sn (a.p.f.u.) and Fe + Nb + Ta + Ti (a.p.f.u.) showing that cassiterite stoichiometry is respected for areas identified by Raman imaging (C), and average content of trace elements in areas identified by Raman imaging (D, see Table 2) expressed in atom per formula unit (a.p.f.u) for the understanding of the substitution in the mineral.

Contribution of RISE confocal Raman imaging integrated in a SEM

Raman spectroscopy provides qualitative information on the presence and distribution of trace elements in cassiterite, based on the presence, intensity and position of Raman bands. The characteristic Raman bands for SnO_2 are the A_{1G} band at 638 rel. cm^{-1} and B_{1G} band at 741 rel. cm^{-1} (Fig. 7B). They correspond to the symmetric and asymmetric stretching of the Sn–O bonds, respectively. Upon incorporation of different elements in the crystal lattice, shifts, broadenings and the appearance of additional Raman bands in the Raman spectrum will occur. According to Wang and co-authors (Wang *et al.*, 1993), a variation of several peaks in Raman shift intensity is observed for the trace element ratio (Nb + Ta)/(Fe + Mn).

The primary problem for Raman analysis on such a cassiterite grain is related to the location of the region of interest, which cannot be analysed – or at least not easily – by optical microscopy. As a result, SEM SE (secondary electrons), BSE (backscattered electrons) and CL imaging were used to determine the precise location of the area of interest (mainly based on the colocation of cracks in the selected area). After locating the region of interest, the sample was transferred inside the vacuum chamber to the confocal Raman measuring position for further analysis. A Raman image (200 × 200 μm^2) was collected from the region of interest, by acquiring a 2D array of 200 × 200 complete Raman spectra with an integration time of 0.08 s per spectrum. The total acquisition time for the Raman image consisting of 40 000 spectra was 53 minutes. The 2D array of Raman spectra was analysed with multivariate spectral analysis methods such as Cluster Analysis, described in details by Dieing & Ibach (2010) The Raman spectra obtained from these analysis are presented in Figure 7(A). All

four spectra contain the main A_{1G} band at 638 rel. cm^{-1} indicating the presence of SnO_2 in the analysed crystal. The distribution of the four components in the analysed sample area is presented in the colour-coded Raman image (Fig. 7A). The colours in the Raman image match the colours of the Raman spectra. As shown previously, based on EBSD and EPMA analyses, this part of the grain is characterised by different areas including main/twin crystal orientation and high/low trace element concentrations. The overlay of the Raman image with the CL image (Fig. 7A) highlights the sensitivity of Raman spectroscopy to grain orientation and incorporation of trace elements in the crystal structure of SnO_2.

Beside the SnO_2 characteristic Raman bands, the spectrum in Figure 7(B) (spectrum d) contains a Raman band at 840 rel. cm^{-1} which can be associated to the A_n vibrational mode of Nb (Wang *et al.*, 1993). By comparing the Raman image (Fig. 7A) with the elemental distribution of Nb (Fig. 6B), a clear correlation can be made. On the other hand, the A_n band is weak or not visible on the green and purple spectra (Fig. 7B spectra a and c), those corresponding to a low Nb content. Low Nb coupled with a low Ti concentration is observed for the purple area (Fig. 7A and Fig. 7B spectrum a), and low Nb coupled with a high Ti concentration is noted for the green area (Fig. 7A and Fig. 7B spectrum c). The B_{2g} band at 741 cm^{-1} is strong on the purple spectrum (Fig. 7B spectrum a) and quite weak on the green one (Fig. 7B spectrum c). The intensity of this band is high compared to the A_n band when characterised by a medium to high Nb content associated with Ta (±Fe) and a low Ti content (purple and blue spectra – Fig. 7B spectra a and d). In the opposite case, the intensity of the B_{2g} band is low compared to the A_n band when Nb and Ta contents are low and Ti is high (green spectrum – Fig. 7B spectrum c). According to Izoret *et al.* (1985), the substitution Sn–Ti in cassiterite is isomorphic and homovalent (Sn^{4+}/Ti^{4+}) whereas at the other end, the Sn–(Nb,Ta) substitution is heterovalent (Sn^{4+}/Nb^{5+},Ta^{5+}) with the necessity of local charge compensation (for example with Fe^{3+}).

In addition, according to EPMA map of tungsten W (data not shown), the blue spectrum (Fig. 7B spectrum b) could be attributed to wolframite.

Thus a relationship can be established between these Raman spectral differences and trace element contents, which agree with the conclusions of Wang and co-authors (Wang *et al.*, 1993). RISE imaging enables a direct link of Raman spectra to trace element distribution and crystal orientation at the micrometric/submicrometric scale in SnO_2 minerals.

Conclusion

In this study, cassiterite zonation and orientation was explored using a panel of SEM-based imaging and microanalysis techniques. The panchromatic intensity of cathodoluminescence of a cassiterite grain is affected by both crystal orientation and trace element distribution. The correlation of CL intensity with crystallographic orientation (EBSD) and trace element distribution (EPMA) can be clearly identified and the influence of each element can be defined at the micrometric scale. The influence of trace elements on luminescence intensity is clearly established.

In addition, we present the benefits of using confocal Raman imaging integrated in a SEM (RISE microscopy). Cassiterite grain analyses on the same area show the complementarity between the various analyses and observations performed by SEM-CL imaging, crystallographic observations (EBSD), elemental analyses and trace element distribution (EPMA) and confocal Raman spectroscopy/imaging. The advantage of using RISE imaging and spectroscopy at a submicrometric scale has been highlighted because of its ability to detect, discriminate and characterise submicrometric areas and phases present in a complex cassiterite grain (down to less than 400 nm according to Jiruse *et al.*, 2014), in correlation with trace elements and crystallographic orientation. The presence of Ta and Nb (heterovalent substitution) correlates with increased A_n (~840 cm^{-1}) and B_{2g} (~741 cm^{-1}) band intensities, whereas the Raman spectrum of an area with a low Nb and Ta coupled with a high Ti content (homovalent substitution) appears to exhibit low intensity A_n and B_{2g} bands. The combination of data collected from the different techniques makes it possible to link directly both chemical and crystallographic data and the changes in the Raman spectrum of cassiterite.

References

Autrata, R. (1992) Single crystal detector suitable for high resolution scanning electron microscopy. *EMSA Bull.* **22**, 54–58.

Ballevre, M., Le Goff, E. & Hebert, R. (2001) The tectonothermal evolution of the Cadomian belt of northern Britanny, France: a Neoproterozoic volcanic arc. *Tectonophysics* **331**, 19–43.

Botelho, N.F. & Moura, M.A. (1998) Granite-ore deposit relationships in Central Brazil. *J. South Am. Earth Sci.* **11**(5), 427–438.

Briskey, J.A. (2005) Indium in zinc-lead and other mineral deposits: a reconnaissance survey of 1118 indium analyses published before 1985. U.S. Geological Survey Open-File Report, 2005–1209.

Cerny, P., Roberts, W.L., Ercit, T.S. & Chapman, R. (1985) Wodginite and associated oxide minerals from the Peerless pegmatite, Pennington County, South Dakota. *Am. Miner.* **70**, 1044–1049.

Chauris, L., Lulzac, Y. & Cotten, J. (1989) Une lame de granite albitique tardi-cadomienne: le gisement stanno-wolframifère de Montbelleux (Massif armoricain, France). *Chronique de la Recherche Minière.* **496**, 25–39.

Das, S. & Hendry, M.J. (2011) Application of Raman spectroscopy to identify Iron minerals commonly found in mine waste. *Chem. Geol.* **290**, 101–108.

Dieing, T. & Ibach, W. (2010) Software requirements and data analysis in confocal Raman microscopy. *Springer Series in Optical Sciences 158* (ed. by T. Dieing, O. Hollricher & J. Toporski). Springer-Verlag, Berlin, Heidelberg.

Everhart, T.E. & Thornley, R.F.M. (1960) Wide-band detector for micro-microampere low-energy electron currents. *J. Sci. Instr.* **37**, 246–248.

Farmer, C.B., Searl, A. & Halls, C. (1991) Cathodoluminescence and growth of cassiterite in the composite lodes at south Corfty Mine, Cornwall, England. *Mineral. Magaz.* **55**, 447–458.

Gao, T., Fjellvag, H. & Norby, P. (2009) A comparison study of Raman scattering properties of α- and β-MnO_2. *Anal. Chim. Acta* **648**, 235–239.

Giuliani, G. (1987) La cassitérite zonée du gisement de Sokhret Allal (Granite des Zaër; Maroc Central): composition chimique et phases fluides associées. *Miner. Depos.* **22**, 253–261.

Hall, A.J. (1978) Post-growth readjustment of a cassiterite twin-boundary revealed by cathodoluminescence. *Mineralog. Magaz.* **42**, 288–290.

Hall, M.R. & Ribbe, P.H. (1971) An electron microprobe study of luminescence centers in cassiterite. *Am. Mineralog.* **56**, 31–45.

Hope, G.A., Wood, R. & Munce, C.G. (2001) Raman microprobe mineral identification. *Min. Eng.* **14**(12), 1565–1577.

Izoret, L., Marnier, G. & Dusausoy, Y. (1985) Caracterisation cristallochimique de la cassiterite des gisements d'etain et de tungstene de Galice, Espagne. *Canad. Miner.* **23**, 221–231.

Jacka, M., Zadrazil, M. & Lopour, F. (2003) A differentially pumped secondary electron detector for low-vacuum scanning electron microscopy. *Scanning* **25**, 243–246.

Jarvis, R.M., Brooker, A. & Goodacre, R. (2004) Surface-enhanced Raman spectroscopy for bacterial discrimination utilizing a scanning electron microscope with a Raman spectroscopy interface. *Anal. Chem.* **76**, 5198–5202.

Jarvis, R.M. & Goodacre, R. (2004) Discrimination of bacteria using surface-enhanced Raman spectroscopy. *Anal. Chem.* **76**, 40–47.

Jiruše, J., Haničinec, M., Havelka, M., Hollricher, O., Ibach, W. & Spizig, P. (2014) Integrating focused ion beam–scanning electron microscope with confocal Raman microscope into a single instrument. *J. Vac. Sci. Technol. B* **32**, 06FC03-1–06FC03-6.

Lahfid, A., Beyssac, O., Deville, E., Negro, F., Chopin, C. & Goffé, B. (2010) Evolution of the Raman spectrum of carbonaceous material in low-grade metasediments of the Glarus Alps (Switzerland). *Terra Nova* **22**, 354–360.

Lerouge, C., Deschamps, Y., Piantone, P., Gilles, C. & Breton, J. (2007) Metal-carrier accessory minerals associated with W ± Sn mineralization, La Châtaigneraie tungsten ore district, Massif Central, France. *Canad. Miner.* **45**, 875–889.

Lerouge, C., Gloaguen, E., Wille, G. & Bailly, L. (2017) The distribution of In and other rare metals in cassiterite and associated minerals in Sn ± W ore deposits of the Western Variscan Belt. *Euro. J. Miner.* **29**, 739–753.

Lloyd, G.E. (1987) Atomic number and crystallographic contrast images with the SEM, a review of backscattered electron techniques. *Mineralog. Magaz.* **51**, 3–19.

Maubec, N., Lerouge, C., Lahfid, A., Wille, G., Michel, K. & Bourrat, X. (2013) Coupled SEM-microRaman system: a powerful tool to characterize a micrometric aluminum-phosphate–sulfate (APS). *J. Mol. Struct.* **1048**, 33–40.

Möller, P., Dulski, P., Szacki, W., Malow, G. & Riedel, E. (1988) Substitution of tin in cassiterite by tantalum, niobium, tungsten, iron and manganese. *Geochim. Cosmochim. Acta* **52**, 1497–1503.

Mossbrucker, J. & Grotjohn, T.A. (1996) Determination of local crystal orientation of diamond using polarized Raman spectra. *Diam. Related Mater.* **5**, 1333–1343.

Mossbrucker, J. & Grotjohn, T.A. (1997) Determination of the components of stress in a polycrystalline diamond film using polarized Raman spectroscopy. *J. Vac. Sci. Technol. A: Vac., Surf. Films* **15**(3), 1206.

Murciego, A., Garcia Sanchez, A., Dusausoy, Y., Martin Pozas, J.M. & Ruck, R. (1997) Geochemistry and EPR of cassiterite from the Iberian Hercynian Massif. *Mineralog. Magaz.* **61**(3), 357–365.

Neiva, A.M.R. (1996) Geochemistry of cassiterite and its inclusions and exsolution products from tin and tungsten deposits in Portugal. *Canad. Miner.* **34**, 745–768.

Nelson, M.P., Zugates, C.T., Treado, P.J., Casuccio, G.S., Exline, D.L. & Schlaegle, S.F. (2001) Combining Raman chemical imaging and scanning electron microscopy to characterize ambient fine particulate matter. *Aer. Sci. Technol.* **34**, 108–117.

Nespolo, M. & Souvignier, B. (2015) Structural rationale for the occurrence of the elbow twins in cassiterite and rutile. *J. Mineral. Petrolog. Sci.* **110**, 157–165.

Otieno-Alego, V. (2009) Some forensic applications of a combined micro-Raman and scanning electron microscopy system. *J. Raman Spectrosc.* **40**, 948–953.

Pointurier, F. & Marie, O. (2010) Identification of the chemical forms of uranium compounds in micrometer-size particles by means of micro-Raman spectrometry and scanning electron microscope. *Spectrochim. Acta Part B – Atomic Spectrosc.* **65**, 797–804.

Remond, G., Cesbron, F., Chapoulie, R., Ohnenstetter, D., Roques-Carmes, C. & Schvoerer, M. (1992) Cathodoluminescence applied to the microcharacterization of mineral materials: a present status in experimentation and interpretation. *Scann. Microsc.* **6**(1), 23–68.

Remond, G. (1973) Exemples d'identification et de localisation des elements en traces dans les minéraux luminescents (cassiterites), à l'aide de l'analyseur ionique. *Bull. Soc. Fran. Miner. Cristallogr.* **96**, 183–198.

Rossi, P., Cocherie, A., Meyer, G., Fouillac, A.M. & Autran, A. (1988) Metallogenic W and Sn granites: genesis and main distinguishing features. *Mineral Deposits within the European Community* (ed. by J. Boissonnas & P. Omenetto). Special Publication No. 6 of the Society for Geology Applied to Mineral Deposits, vol 6. Springer, Berlin, Heidelberg.

Serranti, S., Ferrini, V., Masi, U. & Cabri, L.J. (2002) Trace-element distribution in cassiterite and sulfides from rubané and massive ores of the Corvo deposit, Portugal. *Canad. Miner.* **40**, 815–835.

Stefaniak, E.A., Alsecz, A., Frost, R., Mathe, Z., Sajo, I.E., Torok, S., Worobiec, A. & VanGrieken, R. (2009) Combined SEM/EDX and micro-Raman spectroscopy analysis of uranium minerals from a former uranium mine. *J. Hazard. Mater.* **168**(1), 416–423.

Stefaniak, E.A., Pointurier, F., Marie, O., Truyens, J. & Aregbe, Y. (2014) In-SEM Raman microspectroscopy coupled with EDX – a case study of uranium reference particles. *Analyst* **139**(3), 668–675.

Van Apeldoorn, A.A., Aksenov, Y., Stigter, M. *et al.* (2005) Parallel high-resolution confocal Raman SEM analysis of inorganic and organic bone matrix constituents. *J. R. Soc. Interf.* **2**(2), 39–45.

Wang, R., Wu, J., Dubessy, J. & Monchoux, P. (1993) Raman spectroscopy of Nb, Ta-rich cassiterite in Beauvoir and Montebras Granites. *Fran.–Chin. J. Geochem.* **12**(4), 353–360.

Wille, G., Bourrat, X., Maubec, N. & Lahfid, A. (2014) Raman-in-SEM, a multimodal and multiscale analytical tool: performance for materials and expertise. *Micron* **67**, 50–64.

Worobiec, A., Potgieter-Vermaak, S., Brooker, A., Darchuk, L., Stefaniak, E. & VanGrieken, R. (2010) Interfaced SEM/EDX and micro-Raman Spectrometry for characterisation of heterogeneous environmental particles – fundamental and practical challenges, R. *Microchem. J.* **94**(1), 65–72.